crystals

MDPI

Article

The Effect of Annealing on the Optoelectronic Properties and Energy State of Amorphous Pyrochlore $Y_2Ti_2O_7$ Thin Layers by Sol–Gel Synthesis

Hsiang-An Ting [1], Yong-Yu Chen [2], Zong-Ming Li [2], Ya-Ping Hsieh [3], Sheng-Kuei Chiu [4,*] and Chu-Chi Ting [2,5,*]

1 Department of Electrical Engineering, Institute of Electronics, National Yang Ming Chiao Tung University, Hsinchu 30010, Taiwan; hating.ee10@nycu.edu.tw
2 Department of Mechanical Engineering, Institute of Opto-Mechatronics, National Chung Cheng University, Chiayi 62301, Taiwan; z5484876@alum.ccu.edu.tw (Y.-Y.C.); zed05370882@alum.ccu.edu.tw (Z.-M.L.)
3 Institute of Atomic and Molecular Sciences, Academia Sinica, Taipei 10617, Taiwan; yphsieh@gate.sinica.edu.tw
4 Department of Materials Science and Engineering, Feng Chia University, Taichung 40724, Taiwan
5 Advanced Institute of Manufacturing with High-Tech Innovations, National Chung Cheng University, Chiayi 62301, Taiwan
* Correspondence: skuechiu@fcu.edu.tw (S.-K.C.); ccting@ccu.edu.tw (C.-C.T.)

Abstract: Pyrochlore titanate ($Y_2Ti_2O_7$) is a promising material for a wide range of applications in optoelectronics and photocatalysis due to its advantageous chemical, mechanical, and optical properties. To enhance its potential for such uses, however, a high-quality and scalable synthesis method is required. We here investigate the crystallization of sol–gel produced $Y_2Ti_2O_7$ layers. We observe a transition of the amorphous pyrochlore phase at annealing temperatures below 700 °C. The transmittances of the $Y_2Ti_2O_7$ thin layers annealed at 400 to 700 °C are approximately 92.3%. The refractive indices and packing densities of $Y_2Ti_2O_7$ thin layers annealed at 400–700 °C/1 h vary from 1.931 to 1.954 and 0.835 to 0.846, respectively. The optical bandgap energies of $Y_2Ti_2O_7$ thin layers annealed at 400–700 °C/1 h reduce from 4.356 to 4.319 eV because of the Moss–Burstein effect. These good electronic and optical properties make $Y_2Ti_2O_7$ thin layers a promising host material for many potential applications.

Keywords: pyrochlore; $Y_2Ti_2O_7$; amorphous; sol–gel deposition; refractive index; bandgap energy; packing density

check for updates

Citation: Ting, H.-A.; Chen, Y.-Y.; Li, Z.-M.; Hsieh, Y.-P.; Chiu, S.-K.; Ting, C.-C. The Effect of Annealing on the Optoelectronic Properties and Energy State of Amorphous Pyrochlore $Y_2Ti_2O_7$ Thin Layers by Sol–Gel Synthesis. *Crystals* **2022**, *12*, 564. https://doi.org/10.3390/cryst12040564

Academic Editors: Wei-Chun Lin, Yi-Hsin Chien, Hsiang-Chiu Wu, Po-Kang Yang and Dmitry Medvedev

Received: 10 March 2022
Accepted: 14 April 2022
Published: 18 April 2022

1. Introduction

Pyrochlore titanate ($Y_2Ti_2O_7$) is an important material because it has high mechanical [1,2], chemical [3], thermal stability [4,5], low phonon energy [4,6], good photocatalytic activity [7], a high refractive index [8], and excellent ion-electron conductivity [9,10], etc. Therefore, it has many applications, such as photocatalyst [11], solid-electrolytes of fuel cells [12,13], gas-sensing materials [14], high-K dielectrics [15,16], H_2 storage material [17], nuclear waste storage material [18], transistor device [19], and photovoltaic material [20]. Moreover, $Y_2Ti_2O_7$ can act as the host matrix of phosphor materials. The rare earth-doped $Y_2Ti_2O_7$ have attracted many researchers to pay attention to the application of fiber amplifiers [21], integrated electronic devices [22], up-conversion luminescence temperature sensing material [23–25], and visible up-conversion luminescent solar converter (LSC) in recent years [26].

To realize these applications, a large-scale synthesis approach is needed. To date, $Y_2Ti_2O_7$ nanocrystals or thin films have been produced by several approaches, such as coprecipitation [27,28], hydrothermal processes [29], mechanical milling [30,31], the liquid

mix technique [32], solid-state reaction [33,34], sol–gel processes [14,35,36], and aerosol-assisted chemical vapor deposition (AACVD) [20]. However, certain processes are not readily scalable due to stringent process conditions and complex preparation.

Sol–gel processes, on the other hand, have demonstrated the potential to produce large scale thin films using simple tools, such as printing and spin-coating. Such films are then annealed at high temperatures to enhance their performance.

We here systematically investigate the effects of annealing temperatures on the phase development, layer morphology, and related optoelectronic properties of $Y_2Ti_2O_7$ thin layers. We demonstrate that $Y_2Ti_2O_7$ thin layers have high average transmittance (73.8–75.1%), high refractive index (1.931–1.954 at λ = 550 nm), and high bandgap energy (4.319–4.356 eV), which depends on the variation of annealing temperatures (400–750 °C). Utilizing this understanding, we were able to produce high-quality $Y_2Ti_2O_7$ thin layers directly on a glass substrate. The good optoelectronic properties and scalable production open up new directions for $Y_2Ti_2O_7$-based applications.

2. Experimental Procedures

2.1. Fabrication of Sol–Gel Solution and Thin Layers

Titanium solution was prepared by mixing acetic acid (HAc, 99.9%, Merck, Darmstadt, Germany), titanium isoproxide (≥99%, Acros, Geel, Belgium), and 2-methoxyethanol (2-MOE, 99.9%, Merck) in a molar ratio of Ti/HAc/2-MOE = 1/15/10. Yttrium solution was produced by mixing methanol (Me, ≥99.9%, Merck), ethylene glycol (EG, ≥99.9%, Alfa, Lancashire, UK), and yttrium acetate ($Y(CH_3COO)_3 \cdot 4H_2O$, 99.9%, Alfa) with molar ratio of Y/Me/EG = 1/50/15 and dissolved into the titanium solution. Homogeneous hydrolysis reaction were completed by stirring the mixture solution for 10 h [37,38].

Subsequently, the $Y_2Ti_2O_7$ precursor solution was spin-coated on a Corning 7059 glass substrate at 1000 rpm for 10 s and then 3000 rpm for 30 s. Heating to 120 °C was conducted to dry the deposited sol–gel film. The dried sol–gel films were then pyrolyzed at 380 °C for 50 min in ambient atmosphere.

The sol–gel coating process and subsequent pyrolysis process was repeated eight times to obtain films of approximately 430 nm thickness. Afterwards, thin layers were annealed from 400 to 750 °C for 1 h in ambient conditions. The average layer thickness of 400 ± 10 nm and other property calculations (grain size, transmittance, refractive index, and optical bandgap) were obtained by averaging over five samples.

2.2. Characterization of Thin Layers

The α-step profile meter (Alpha-Step IQ, KLA-Tencor, Milpitas, CA, USA) is utilized for the thickness of thin layers' measurements. A scanning electron microscopy (SEM) (Hitachi, Tokyo, Japan, S4800-I) was performed at an accelerating voltage of 15 kV. A Shimadzu UV-2100 spectrophotometer was used for transmission spectra measurement of the $Y_2Ti_2O_7$ thin layer in the UV-visible range. X-ray diffraction (XRD) measurements of thin layers were performed by an X-ray diffractometer (Bruker, Billerica, MA, USA, D8 discovery) with CuKα radiation (λ = 0.154 nm).

3. Results and Discussion

3.1. Crystal Structure and Layer Morphology

The XRD patterns in Figure 1 show the effect of annealing at different temperatures (400, 500, 600, 700, and 750 °C) for 1 h on the phase transformation of $Y_2Ti_2O_7$ thin layers. For the annealing temperatures ≤ 700 °C, $Y_2Ti_2O_7$ thin layers exhibit a weak broad continuum around 2θ = ~30° ((222) peak) which is the characteristic of an amorphous structure exhibiting short-range order. When the annealing temperature reaches 750 °C, the well-crystallized pyrochlore phase is identified by the (222), (311), (400), and (622) peaks (JCPDS No. 42-0413). No TiO_2, Y_2O_3, and other phases are observed in this system. This transition temperature between amorphous and crystalline $Y_2Ti_2O_7$ is in the range of previous reports on sol–gel processes, e.g., 725 [39], 750 [40], or 800 °C [35,36]. However,

the other sol–gel or AACVD methods can induce the formation of crystallized $Y_2Ti_2O_7$ phase at 550–570 °C [14,20]. The different starting materials and processes can result in the different crystalized temperatures and crystallinity.

The average grain size (D) of $Y_2Ti_2O_7$ thin layers is determined by the Scherrer equation [41]:

$$D = \frac{S\lambda}{\sqrt{B_M - B_S}\cos\theta} \quad (1)$$

where S is the Scherrer constant (0.9), λ is the wavelength of incident radiation, θ is the Bragg angle corresponding to the XRD peak being considered. B_M and B_S are the width in radians of one of the sample and standard (Si powder) diffraction peaks at half-maximum, respectively. The instrument broadening (B_S) is 0.14 in our system.

After calculation, the average estimated grain sizes of the $Y_2Ti_2O_7$ thin layers annealed at 600, 700 and 750 °C for 1 h are ~1.4 nm, ~1.5 nm, and ~32 nm, respectively. It is worth noting that the intensity of the broad (222) peak gradually increases when the annealing temperature increases from 400 to 700 °C. Furthermore, the crystals grow up and the XRD peak of the (222) facet becomes sharper at 750 °C. This means that the portion of amorphous $Y_2Ti_2O_7$ phase reduces as the crystallinity of $Y_2Ti_2O_7$ phase is enhanced. Due to the glass transition temperature of the Corning 7059 substrate, the annealing temperature range is limited to 750 °C.

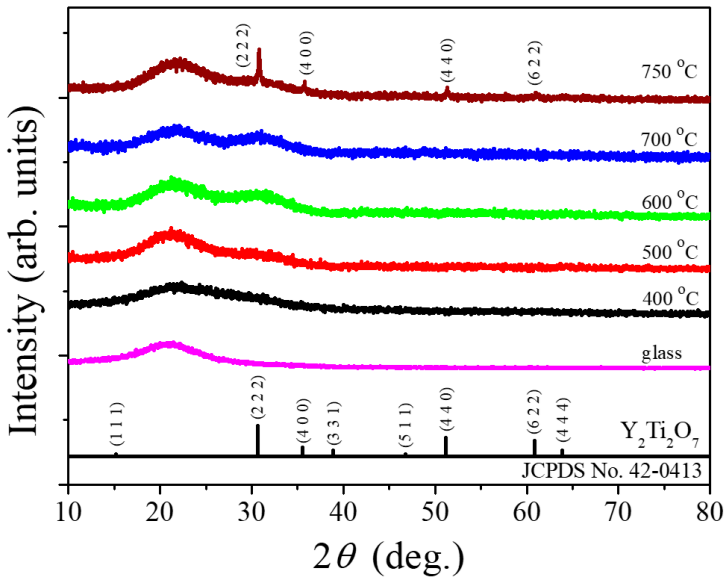

Figure 1. XRD patterns of the $Y_2Ti_2O_7$ thin layers annealed at the temperatures of 400 to 750 °C for 1 h. The 2θ positions for bulk $Y_2Ti_2O_7$ are shown on the plot for the reference.

Figure 2 represents top-view SEM images of the $Y_2Ti_2O_7$ thin layers annealed at 400, 500, 600, 700, and 750 °C for 1 h. No crystal facets or signs of grain boundaries were detected when samples were annealed below 750 °C. This absence is expected from our XRD analysis, as the grain size of these films is below the resolution of the SEM. Conversely, crystal structures and grain boundaries can be observed at 750 °C annealing. As the surface of sol–gel spin coating thin films is very smooth, SEM images are not very clear.

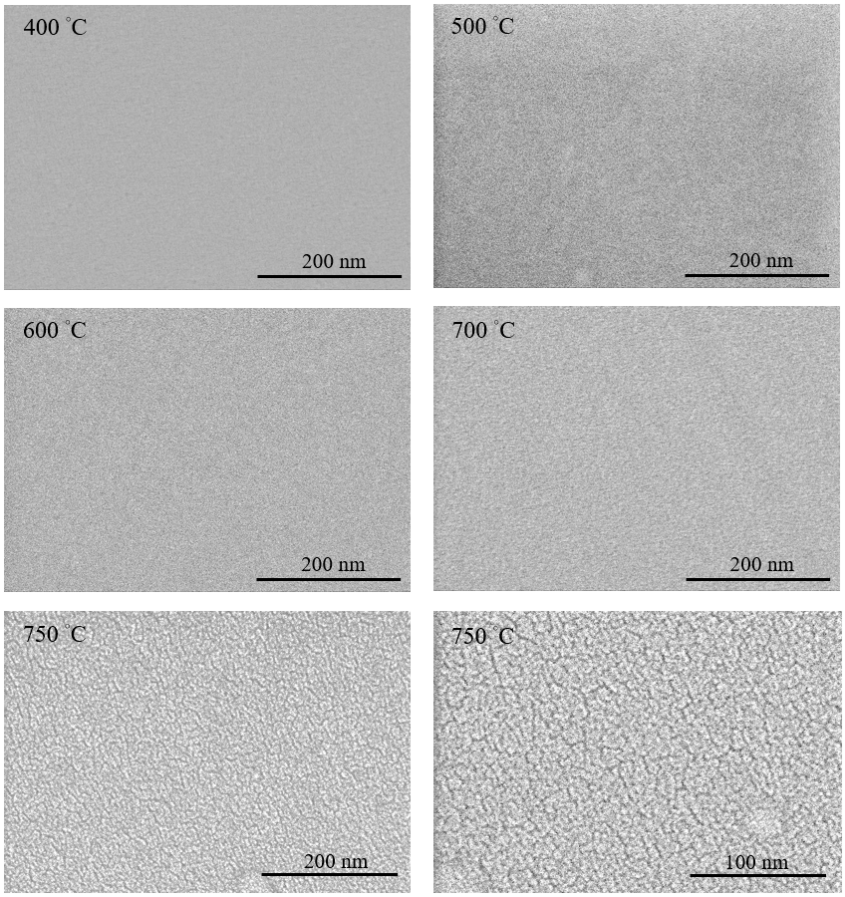

Figure 2. Top-view SEM imagines of the $Y_2Ti_2O_7$ thin layers annealed at 400, 500, 600, 700, and 750 °C for 1 h (magnification: 200 K—400–750 °C, 300 K—750 °C).

3.2. Optoelectronic Properties

Figure 3 shows the effect of annealing temperatures on the transmittance spectra of the $Y_2Ti_2O_7$ thin layers annealed at 400, 500, 600, 700, and 750 °C for 1 h. The small fluctuation at high transmittances is due to the Fabry–Perot interference phenomenon of multiple reflected beams.

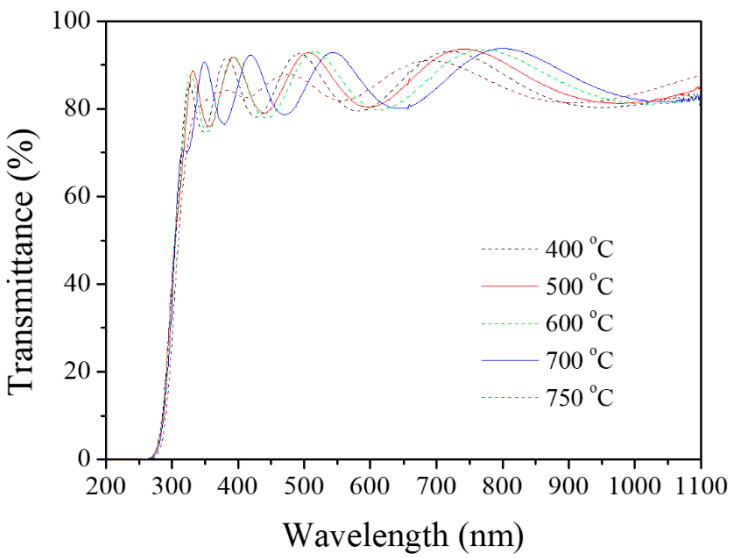

Figure 3. Transmittance spectra of the $Y_2Ti_2O_7$ thin layers annealed at the temperatures of 400 to 750 °C for 1 h.

For $Y_2Ti_2O_7$ thin layers annealed at 400, 500, 600, and 700 °C, the regular interference fringes indicate that all of the $Y_2Ti_2O_7$ thin layers have smooth interfaces and surfaces. The transmittance peaks of difference annealing temperatures slightly shift. Thin layers with different refractive indices result in the different optical path lengths for the constructive/destructive interference. However, $Y_2Ti_2O_7$ thin layers annealed at 750 °C exhibit more random interference. This effect originates from the surface melting of the glass substrate and other optical properties (transmittance, optical bandgap, and refractive index) of $Y_2Ti_2O_7$ thin layers annealed at 750 °C cannot be calculated.

The maximum transmittances in the wavelength ranging 200–1100 nm of the $Y_2Ti_2O_7$ thin layers annealed at 400–700 °C/1 h are approximately 92.3%. These amorphous thin layers have small grain size and low surface roughness resulting in the weak scattering and high transmittance.

The refractive index (n) of the $Y_2Ti_2O_7$ thin layer can be obtained from the transmittance spectra by fit to the Swanepoel and Cauchy equation [42]. Figure 4 shows the wavelength dependence of refractive indices for $Y_2Ti_2O_7$ thin layer annealed at 400, 500, 600, and 700 °C for 1 h. As the annealing temperature increases, the refractive index of the thin layer increases. The refractive indices are 1.931, 1.936, 1.941, and 1.954 at λ = 550 nm for $Y_2Ti_2O_7$ thin layers annealed at 400, 500, 600, and 700 °C for 1 h, respectively. At higher temperatures, the crystallinity and densification of $Y_2Ti_2O_7$ thin layers are also improved, which leads the higher refractive indices of $Y_2Ti_2O_7$ thin layers. On the other hand, the refractive index of the amorphous phase is usually lower than that of high crystalline phase (e.g., the refractive index of bulk $Y_2Ti_2O_7$ is 2.34) [43].

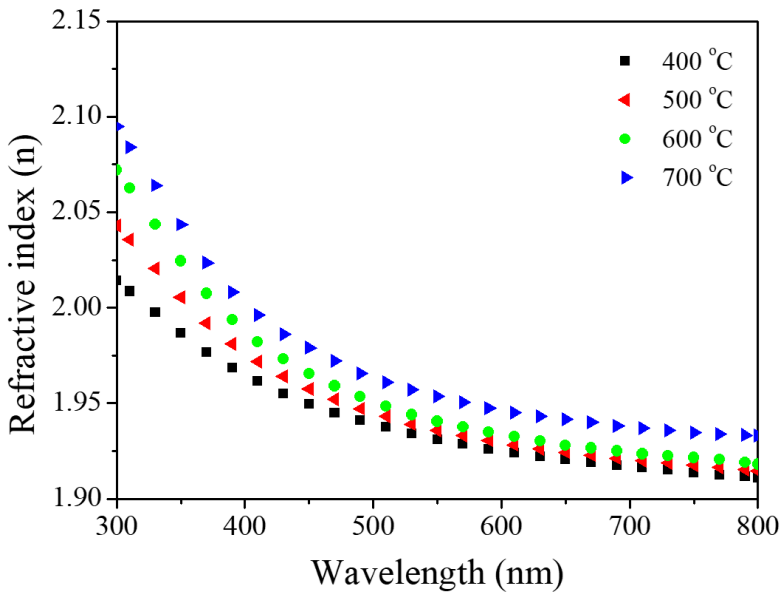

Figure 4. Wavelength dependence of the refractive index for the $Y_2Ti_2O_7$ thin layers annealed at 400, 500, 600, and 700 °C for 1 h.

In addition, we calculate the degree of porosity in $Y_2Ti_2O_7$ thin layers. By following the Bragg–Pippard formula [44], the packing density (P) can be calculated using the following equation:

$$n_f{}^2 = \frac{(1-P)n_v{}^4 + (1+P)n_p{}^2 n_b{}^2}{(1+P)n_v{}^2 + (1-P)n_b{}^2} \quad (2)$$

where n_v, n_b and n_f are the refractive indices of voids (n_v = 1 for empty voids), bulk materials, and porous layers, respectively. The packing densities of the $Y_2Ti_2O_7$ thin layers annealed at 400, 500, 600, and 700 °C for 1 h are 0.835, 0.837, 0.84, and 0.846, respectively. The packing density increases with annealing temperature, which is attributed to the significant increase in the crystallinity and reduction in the porosity.

Figure 5 plots the relationship of $(\alpha h\nu)^2$ versus photon energy (E) of the $Y_2Ti_2O_7$ thin layers annealed at 400–700 °C/1 h, and the extrapolated optical bandgap energies of thin layers were determined.

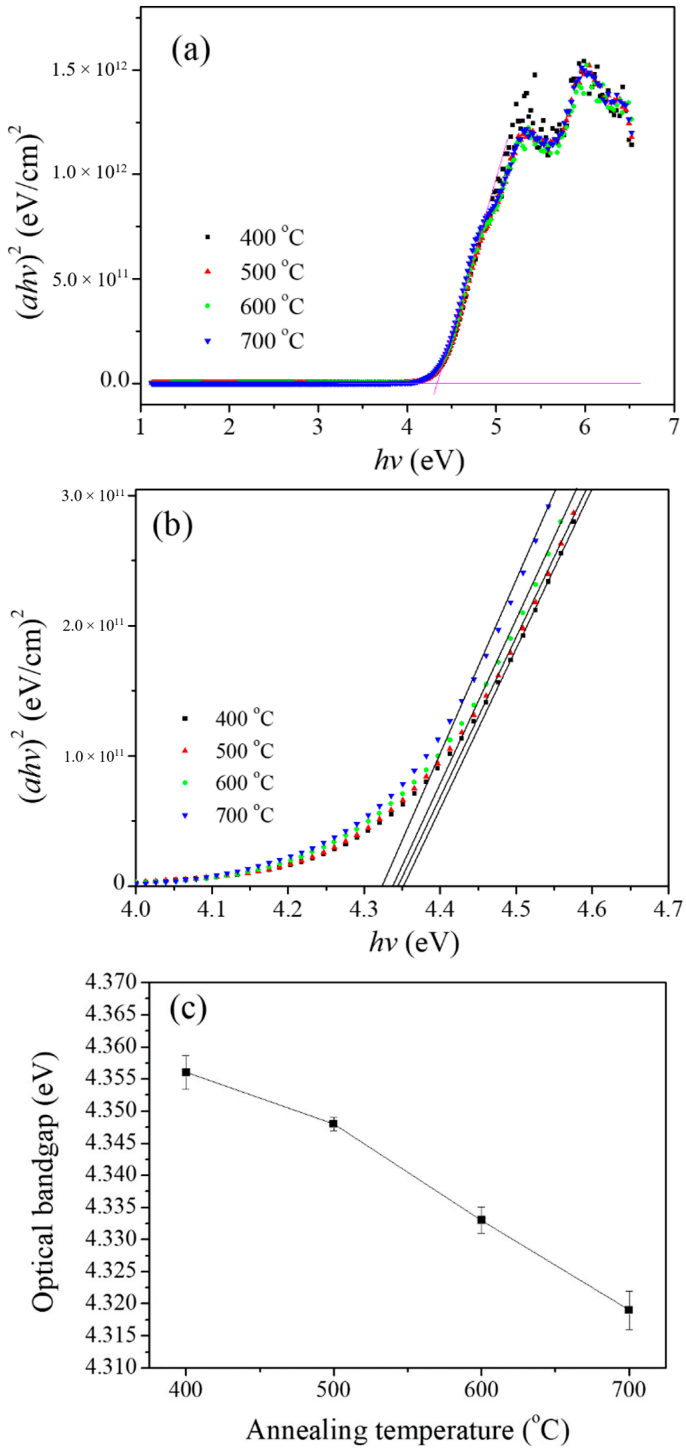

Figure 5. (**a**) $(\alpha h\nu)^2$ as a function of photon energy (E) of the $Y_2Ti_2O_7$ thin layers annealed at 400–700 °C/1 h. (**b**) Enlarged diagram of (**a**). (**c**) Optical bandgap as a function of annealing temperatures. The error bars represent the statistical deviation among five samples.

The optical bandgap energy (Eg) of thin layer can be related to absorption coefficient (α) by Equation (3)

$$\alpha h\nu = \text{const.}\ (h\nu - \text{Eg})^m \quad (3)$$

where m = 1/2, 3/2, 2 or 3 indicates allowed direct, forbidden direct, allowed indirect, and forbidden indirect electronic transitions, respectively [45]. A better linear dependence can be found in the $(\alpha h\nu)^{1/m}$ versus E plots at m = 1/2 for all thin layers, which means the $Y_2Ti_2O_7$ thin layer belongs to direct-transition-type material.

As shown in Figure 5, the optical bandgap energy decrements from 4.356 to 4.319 eV were observed when the $Y_2Ti_2O_7$ thin layers annealing temperatures increase from 400 to 700 °C. These optical bandgap energies are higher than that of the crystallized $Y_2Ti_2O_7$ thin films [14]. There are several causes or aspects, such as grain size [46,47], thickness [46,48], stress [49], and defects [50,51] could affect or shift the bandgap energy of thin layer materials. For the amorphous $Y_2Ti_2O_7$ thin layers annealed from 400 to 700 °C, however, this red shift of bandgap energy could be mainly attributed to defects.

Many defects such as unsaturated bonds, dangling bonds, interstitial atoms, and vacancies can exist in amorphous structure. In general, oxygen vacancies can be observed in many transition metal oxide thin layers such as ZnO [52], $Ba_xSr_{1-x}TiO_3$ [53,54], $CdIn_2O_4$ [55,56], WO_3 [57,58], and TiO_2 [59]. Moreover, enormous oxygen vacancies can exist in the $Y_2Ti_2O_7$ lattice because the large unit cell of $Y_2Ti_2O_7$ allows some of the oxygen ions to move relatively freely, which results in the formation of small polarons [57]. Therefore, oxygen vacancies could be the dominant vacancy defects in amorphous $Y_2Ti_2O_7$ thin layers.

According to the defect reaction equation, two free charge carriers can be generated from the creation of one oxygen vacancy [60]. Like the Moss–Burstein effect, the lowest state of the conduction band is blocked by these free charge carriers, resulting in an increase in the optical bandgap energy [61,62]. After higher temperature annealing, the crystallization of amorphous $Y_2Ti_2O_7$ thin layers was improved with the annihilation of oxygen vacancies, which is associated with the reduction in free charge carriers and the decrease in the optical bandgap energy, as shown in Figure 6.

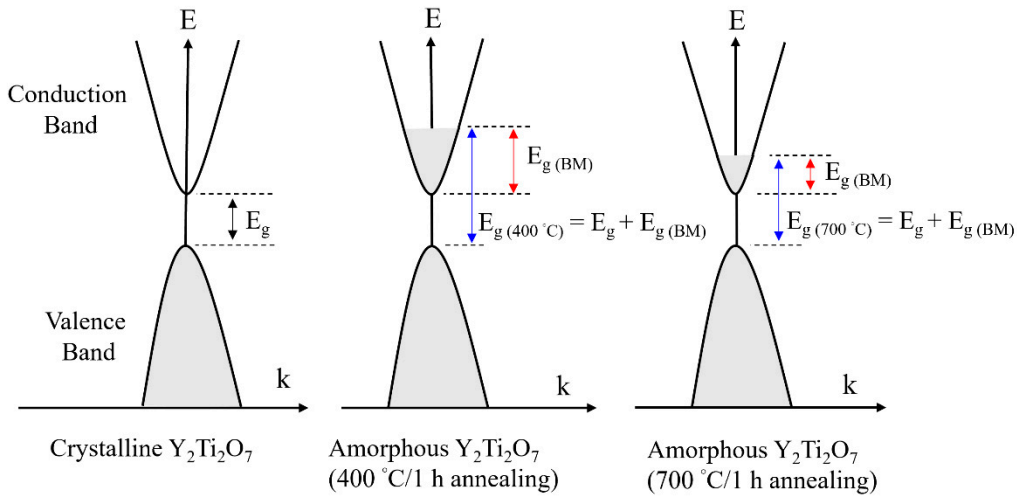

Figure 6. Schematic representation of the Burstein–Moss (B-M) shift for the $Y_2Ti_2O_7$ thin layers annealed at 400 and 700 °C for 1 h.

4. Conclusions

$Y_2Ti_2O_7$ thin layers with a thickness of ~400 nm thin layers were fabricated by the sol–gel technique. At annealing temperatures below 700 °C, all thin layers maintain an amorphous structure. The maximum transmittance of amorphous thin layers is approximately 92.3%. The transmittance is high because of small grain size, low surface roughness, and weak scattering. The refractive indices and optical bandgap energies of $Y_2Ti_2O_7$ thin layers are strongly related to the annealing temperatures. The enlarged refractive indices with the increase in annealing temperatures are attributed to thin layers with the improved densification and crystallinity. The refractive indices (n at λ = 550 nm) of $Y_2Ti_2O_7$ thin layers can be altered from 1.931 to 1.954 as the annealing temperature raises from 400 to 700 °C/1 h.

The amorphous $Y_2Ti_2O_7$ thin layers annealed at higher temperatures possess smaller optical bandgap energy (4.319 eV), which could be attributed to the Burstein–Moss shift.

Author Contributions: Conceptualization, C.-C.T.; Formal analysis, H.-A.T., Y.-Y.C., Z.-M.L. and C.-C.T.; Investigation, H.-A.T., Y.-Y.C., Z.-M.L. and C.-C.T.; Methodology, H.-A.T., Y.-Y.C. and Z.-M.L.; Supervision, C.-C.T.; Validation, C.-C.T.; Writing—original draft, H.-A.T., Y.-Y.C., Z.-M.L. and C.-C.T.; Writing—review & editing, Y.-P.H., S.-K.C. and C.-C.T. All authors have read and agreed to the published version of the manuscript.

Funding: This research was founded by the Ministry of Science and Technology, Taiwan, the Republic of China under Contract No. MOST 108-2221-E-194-001.

Institutional Review Board Statement: Not applicable.

Informed Consent Statement: Not applicable.

Data Availability Statement: The data presented in this study are available on request from the corresponding author.

Conflicts of Interest: The authors declare no conflict of interest.

References

1. Suganya, M.; Ganesan, K.; Vijayakumar, P.; Gill, A.S.; Ramaseshan, R.; Ganesamoorthy, S. Structural, optical and mechanical properties of $Y_2Ti_2O_7$ single crystal. *Scr. Mater.* **2020**, *187*, 227–231. [CrossRef]
2. Zhao, H.; Liu, T.; Bai, Z.; Wang, L.; Gao, W.; Zhang, L. Corrosion behavior of 14Cr ODS steel in supercritical water: The influence of substituting Y_2O_3 with $Y_2Ti_2O_7$ nanoparticles. *Corros. Sci.* **2020**, *163*, 108272. [CrossRef]
3. Badjeck, V.; Walls, M.; Chaffron, L.; Malaplate, J.; March, K. New insights into the chemical structure of $Y_2Ti_2O_7-\delta$ nanoparticles in oxide dispersion-strengthened steels designed for sodium fast reactors by electron energy-loss spectroscopy. *J. Nucl. Mater.* **2015**, *456*, 292–301. [CrossRef]
4. Lai, F.; Cheng, H.; Jiang, Z.; Liu, C.; Liang, T.; You, W. Manipulation of upconversion property and enhancement of sensitivity by tailoring the local structure. *J. Am. Ceram. Soc.* **2021**, *104*, 369–382. [CrossRef]
5. Dai, P.; Zhang, X.; Zhou, M.; Li, X.; Yang, J.; Sun, P.; Xu, C.; Liu, Y. Thermally stable pyrochlore $Y_2Ti_2O_7$: Eu^{3+} orange–red emitting phosphors. *J. Am. Ceram. Soc.* **2012**, *95*, 658–662. [CrossRef]
6. Yu, X.; Zhao, T.; Wang, T.; Bao, W.; Zhang, H.; Su, C. Up-conversion luminescence properties of Ho^{3+}-Yb^{3+} Co-doped transparent glass ceramics containing $Y_2Ti_2O_7$. *J. Non-Cryst. Solids* **2021**, *574*, 121163. [CrossRef]
7. Merka, O.; Bahnemann, D.W.; Wark, M. Improved photocatalytic hydrogen production by structure optimized nonstoichiometric $Y_2Ti_2O_7$. *ChemCatChem* **2012**, *4*, 1819–1827. [CrossRef]
8. Wang, Z.; Wang, X.; Zhou, G.; Xie, J.; Wang, S. Highly transparent yttrium titanate ($Y_2Ti_2O_7$) ceramics from co-precipitated powders. *J. Eur. Ceram. Soc.* **2019**, *39*, 3229–3234. [CrossRef]
9. Yamaguchi, S.; Kobayashi, K.; Abe, K.; Yamazaki, S.; Iguchi, Y. Electrical conductivity and thermoelectric power measurements of $Y_2Ti_2O_7$. *Solid State Ion.* **1998**, *113*, 393–402. [CrossRef]
10. Gill, J.K.; Pandey, O.; Singh, K. Ionic conductivity, structural and thermal properties of pure and Sr^{2+} doped $Y_2Ti_2O_7$ pyrochlores for SOFC. *Solid State Sci.* **2011**, *13*, 1960–1966. [CrossRef]
11. Abe, R.; Higashi, M.; Zou, Z.; Sayama, K.; Abe, Y. Photocatalytic water splitting into H_2 and O_2 over $R_2Ti_2O_7$ (R = Y, rare earth) with pyrochlore structure. *Chem. Lett.* **2004**, *33*, 954–955. [CrossRef]
12. Gill, J.K.; Pandey, O.; Singh, K. Ionic conductivity, structural and thermal properties of Ca^{2+} doped $Y_2Ti_2O_7$ pyrochlores for SOFC. *Int. J. Hydrogen Energy* **2012**, *37*, 3857–3864. [CrossRef]
13. Higashi, M.; Abe, R.; Sayama, K.; Sugihara, H.; Abe, Y. Improvement of photocatalytic activity of titanate pyrochlore $Y_2Ti_2O_7$ by addition of excess Y. *Chem. Lett.* **2005**, *34*, 1122–1123. [CrossRef]
14. Mahapatra, A.; Subudhi, S.; Swain, S.; Sahu, R.; Negi, R.; Samanta, B.; Kumar, P. Electrical and optical properties of yttrium titanate thin films synthesized by Sol-Gel technique. *Integr. Ferroelectr.* **2019**, *203*, 43–51. [CrossRef]
15. Wen, Q.; Zhou, W.; Gao, H.; Zhou, Y.; Luo, F.; Zhu, D.; Huang, Z.; Qing, Y. Enhanced dielectric and microwave absorption properties of $Y_2Ti_2O_7$ ceramics by Sr doping. *Appl. Phys. A* **2019**, *125*, 413. [CrossRef]
16. Öztürk, E.; Sarılmaz, E. The investigation of the photoluminescent and piezoelectric effect of Eu^{3+} doped $Y_2Ti_2O_7$ and $Sm_2Ti_2O_7$ host crystals. *Mater. Chem. Phys.* **2020**, *239*, 122085. [CrossRef]
17. Li, W.; Chuah, C.Y.; Yang, Y.; Bae, T.-H. Nanocomposites formed by in situ growth of NiDOBDC nanoparticles on graphene oxide sheets for enhanced CO_2 and H_2 storage. *Microporous Mesoporous Mater.* **2018**, *265*, 35–42. [CrossRef]
18. Pace, S.; Cannillo, V.; Wu, J.; Boccaccini, D.; Seglem, S.; Boccaccini, A. Processing glass–pyrochlore composites for nuclear waste encapsulation. *J. Nucl. Mater.* **2005**, *341*, 12–18. [CrossRef]
19. Goodenough, J.; Castellano, R. Defect pyrochlores as catalyst supports. *J. Solid State Chem.* **1982**, *44*, 108–112. [CrossRef]

20. Munawar, K.; Mansoor, M.A.; Olmstead, M.M.; Yusof, F.B.; Misran, M.B.; Basirun, W.J.; Mazhar, M. Pyrochlore-structured $Y_2Ti_2O_7$–$2TiO_2$ composite thin films for photovoltaic applications. *J. Aust. Ceram. Soc.* **2019**, *55*, 921–932. [CrossRef]
21. Mondal, K.; Hartman, K.; Dasgupta, D.; Trifon, G.; Dasari, M. Synthesis and characterization of $Y_2Ti_2O_7$ and $ErxY_{2\_}xTi_2O_7$ nanofibers. *J. Sol-Gel Sci. Technol.* **2015**, *73*, 265–269. [CrossRef]
22. Jenouvrier, P.; Boccardi, G.; Fick, J.; Jurdyc, A.-M.; Langlet, M. Up-conversion emission in rare earth-doped $Y_2Ti_2O_7$ sol–gel thin films. *J. Lumin.* **2005**, *113*, 291–300. [CrossRef]
23. Jenouvrier, P.R.; Langlet, M.; Fick, J. High photoluminescence in a new nanocrystalline active phase: YETO. In Proceedings of the Sol-Gel Optics VI. International Symposium on Optical Science and Technology, Seattle, WA, USA, 23 October 2002; pp. 52–59.
24. Tu, X.; Xu, J.; Li, M.; Xie, T.; Lei, R.; Wang, H.; Xu, S. Color-tunable upconversion luminescence and temperature sensing behavior of Tm^{3+}/Yb^{3+} codoped $Y_2Ti_2O_7$ phosphors. *Mater. Res. Bull.* **2019**, *112*, 77–83. [CrossRef]
25. Huang, X.; Huang, K.; Chen, L.; Chen, N.; Lei, R.; Zhao, S.; Xu, S. Effect of Li^+/Mg^{2+} co-doping and optical temperature sensing behavior in $Y_2Ti_2O_7$: Er^{3+}/Yb^{3+} upconverting phosphors. *Opt. Mater.* **2020**, *107*, 110114. [CrossRef]
26. Reisfeld, R.; Saraidarov, T.; Panzer, G.; Levchenko, V.; Gaft, M. New optical material europium EDTA complex in polyvinyl pyrrolidone films with fluorescence enhanced by silver plasmons. *Opt. Mater.* **2011**, *34*, 351–354. [CrossRef]
27. Henkes, A.E.; Bauer, J.C.; Sra, A.K.; Johnson, R.D.; Cable, R.E.; Schaak, R.E. Low-temperature nanoparticle-directed solid-state synthesis of ternary and quaternary transition metal oxides. *Chem. Mater.* **2006**, *18*, 567–571. [CrossRef]
28. Lee, W.J.; Bae, D.S. Synthesis and Characterization of $Y_2Ti_2O_7$ Photocatalytic Powders by Thermal Assist Process. *Defect Diffus. Forum* **2017**, *380*, 86–91. [CrossRef]
29. Gadipelly, T.; Dasgupta, A.; Ghosh, C.; Krupa, V.; Sornadurai, D.; Sahu, B.K.; Dhara, S. Synthesis and structural characterisation of $Y_2Ti_2O_7$ using microwave hydrothermal route. *J. Alloys Compd.* **2020**, *814*, 152273. [CrossRef]
30. Fuentes, A.F.; Boulahya, K.; Maczka, M.; Hanuza, J.; Amador, U. Synthesis of disordered pyrochlores, $A_2Ti_2O_7$ (A = Y, Gd and Dy), by mechanical milling of constituent oxides. *Solid State Sci.* **2005**, *7*, 343–353. [CrossRef]
31. Simondon, E.; Giroux, P.-F.; Chaffron, L.; Fitch, A.; Castany, P.; Gloriant, T. Mechanical synthesis of nanostructured $Y_2Ti_2O_7$ pyrochlore oxides. *Solid State Sci.* **2018**, *85*, 54–59. [CrossRef]
32. Dimesso, L. Pechini processes: An alternate approach of the sol–gel method, preparation, properties, and applications. *Handb. Sol-Gel Sci. Technol.* **2016**, *2*, 1–22.
33. Wang, S.; Wang, L.; Ewing, R.; Kutty, K.G. Ion irradiation of rare-earth-and yttrium-titanate-pyrochlores. *Nucl. Instrum. Methods Phys. Res. Sect. B Beam Interact. Mater. At.* **2000**, *169*, 135–140. [CrossRef]
34. Vishwakarma, P.; Shahi, P.; Rai, S.; Bahadur, A. Low temperature optical sensor based on non-thermally coupled level of Ho^{3+} and defect level of Zn^{2+} in Yb^{3+}: $Y_2Ti_2O_7$ phosphor. *J. Phys. Chem. Solids* **2020**, *142*, 109445. [CrossRef]
35. Chen, Z.; Gong, W.; Chen, T.; Li, S.; Wang, D.; Wang, Q. Preparation and upconversion luminescence of Er^{3+}/Yb^{3+} codoped $Y_2Ti_2O_7$ nanocrystals. *Mater. Lett.* **2012**, *68*, 137–139. [CrossRef]
36. Pavitra, E.; Raju, G.S.R.; Yu, J.S. Solvothermal synthesis and luminescent properties of $Y_2Ti_2O_7$: Eu^{3+} spheres. *Phys. Status Solidi Rapid Res. Lett.* **2013**, *7*, 224–227. [CrossRef]
37. Zhang, X.; Yang, H.; Tang, A. Optical, electrochemical and hydrophilic properties of Y_2O_3 doped TiO_2 nanocomposite films. *J. Phys. Chem. B* **2008**, *112*, 16271–16279. [CrossRef]
38. Guo, J.; Li, J.; Kou, H. Chemical preparation of advanced ceramic materials. In *Modern Inorganic Synthetic Chemistry*; Elsevier: Amsterdam, The Netherlands, 2011; pp. 429–454.
39. Chen, Z.S.; Gong, W.P.; Chen, T.F.; Xiong, G.X.; Huang, G.L. Preparation of $Y_2Ti_2O_7$ nanocrystal by sol-gel method and its characterization. *Adv. Mater. Res.* **2010**, *97*, 2175–2179. [CrossRef]
40. Jenouvrier, P.; Langlet, M.; Rimet, R.; Fick, J. Influence of crystallisation on the photoluminescence properties of $Y_{2-x}Er_xTi_2O_7$ sol-gel thin films. *Appl. Phys. A* **2003**, *77*, 687–692. [CrossRef]
41. Watanabe, T. *Nano-Plating: Microstructure Control Theory of Plated Film and Data Base of Plated Film Microstructure*; Elsevier: Amsterdam, The Netherlands, 2004.
42. Swanepoel, R. Determination of the thickness and optical constants of amorphous silicon. *J. Phys. E Sci. Instrum.* **1983**, *16*, 1214. [CrossRef]
43. Ting, C.-C.; Chiu, Y.-S.; Chang, C.-W.; Chuang, L.-C. Visible and infrared luminescence properties of Er^{3+}-doped $Y_2Ti_2O_7$ nanocrystals. *J. Solid State Chem.* **2011**, *184*, 563–571. [CrossRef]
44. Prathap, P.; Revathi, N.; Subbaiah, Y.V.; Reddy, K.R. Thickness effect on the microstructure, morphology and optoelectronic properties of ZnS films. *J. Phys. Condens. Matter* **2007**, *20*, 035205. [CrossRef]
45. Sinha, G.; Adhikary, K.; Chaudhuri, A. Sol–gel derived phase pure α-Ga_2O_3 nanocrystalline thin film and its optical properties. *J. Cryst. Growth* **2005**, *276*, 204–207. [CrossRef]
46. Lee, S.-M.; Joo, Y.-H.; Kim, C.-I. Influences of film thickness and annealing temperature on properties of sol–gel derived ZnO–SnO_2 nanocomposite thin film. *Appl. Surf. Sci.* **2014**, *320*, 494–501. [CrossRef]
47. Guang-Lei, T.; Hong-Bo, H.; Jian-Da, S. Effect of microstructure of TiO_2 thin films on optical band gap energy. *Chin. Phys. Lett.* **2005**, *22*, 1787. [CrossRef]
48. Bao, D.; Yao, X.; Wakiya, N.; Shinozaki, K.; Mizutani, N. Band-gap energies of sol-gel-derived $SrTiO_3$ thin films. *Appl. Phys. Lett.* **2001**, *79*, 3767–3769. [CrossRef]

49. Peng, L.; Fang, L.; Yang, X.; Li, Y.; Huang, Q.; Wu, F.; Kong, C. Effect of annealing temperature on the structure and optical properties of In-doped ZnO thin films. *J. Alloys Compd.* **2009**, *484*, 575–579. [CrossRef]
50. Xin, G.; Guo, W.; Ma, T. Effect of annealing temperature on the photocatalytic activity of WO_3 for O_2 evolution. *Appl. Surf. Sci.* **2009**, *256*, 165–169. [CrossRef]
51. Kumar, M.; Hazra, S.; Som, T. Role of metallic-like conductivity in unusual temperature-dependent transport in n-ZnO: Al/p-Si heterojunction diode. *J. Phys. D Appl. Phys.* **2015**, *48*, 455301. [CrossRef]
52. Shinde, V.; Lokhande, C.; Mane, R.; Han, S.-H. Hydrophobic and textured ZnO films deposited by chemical bath deposition: Annealing effect. *Appl. Surf. Sci.* **2005**, *245*, 407–413. [CrossRef]
53. Roy, S.C.; Sharma, G.; Bhatnagar, M. Large blue shift in the optical band-gap of sol–gel derived $Ba_{0.5}Sr_{0.5}TiO_3$ thin films. *Solid State Commun.* **2007**, *141*, 243–247. [CrossRef]
54. Saravanan, K.V.; Sudheendran, K.; Krishna, M.G.; Raju, K.J. Effect of the amorphous-to-crystalline transition in $Ba_{0.5}Sr_{0.5}TiO_3$ thin films on optical and microwave dielectric properties. *J. Phys. D Appl. Phys.* **2009**, *42*, 045401. [CrossRef]
55. Wang, Z.; Zou, T.; Xing, X.; Zhao, R.; Wang, Z.; Yang, Y.; Wang, Y. $CdIn_2O_4$ nanoporous thin film gas-sensor for formaldehyde detection. *Phys. E Low-Dimens. Syst. Nanostruct.* **2018**, *103*, 18–24. [CrossRef]
56. Deokate, R.; Bhosale, C.; Rajpure, K. Synthesis and characterization of $CdIn_2O_4$ thin films by spray pyrolysis technique. *J. Alloys Compd.* **2009**, *473*, L20–L24. [CrossRef]
57. Chatten, R.; Chadwick, A.V.; Rougier, A.; Lindan, P.J. The oxygen vacancy in crystal phases of WO_3. *J. Phys. Chem. B* **2005**, *109*, 3146–3156. [CrossRef] [PubMed]
58. Gillet, M.; Lemire, C.; Gillet, E.; Aguir, K. The role of surface oxygen vacancies upon WO_3 conductivity. *Surf. Sci.* **2003**, *532*, 519–525. [CrossRef]
59. Iijima, K.; Goto, M.; Enomoto, S.; Kunugita, H.; Ema, K.; Tsukamoto, M.; Ichikawa, N.; Sakama, H. Influence of oxygen vacancies on optical properties of anatase TiO_2 thin films. *J. Lumin.* **2008**, *128*, 911–913. [CrossRef]
60. Sudo, H.; Nakamura, K.; Maeda, S.; Okamura, H.; Izunome, K.; Sueoka, K. Point Defect Reaction in Silicon Wafers by Rapid Thermal Processing at More Than 1300 °C Using an Oxidation Ambient. *ECS J. Solid State Sci. Technol.* **2019**, *8*, P35. [CrossRef]
61. Peelaers, H.; Van de Walle, C.G. Sub-band-gap absorption in Ga_2O_3. *Appl. Phys. Lett.* **2017**, *111*, 182104. [CrossRef]
62. Li, K.; Gao, Q.; Zhao, L.; Liu, Q. Electrical and Optical Properties of Nb-doped $SrSnO_3$ Epitaxial Films Deposited by Pulsed Laser Deposition. *Nanoscale Res. Lett.* **2020**, *15*, 164. [CrossRef]